



Cite this: *Energy Environ. Sci.*, 2023, 16, 2262

Refined molecular microstructure and optimized carrier management of multicomponent organic photovoltaics toward 19.3% certified efficiency†

Shuixing Li,‡^a Chengliang He,‡^a Tianyi Chen,‡^a Jiale Zheng,‡^b Rui Sun, ID^c Jin Fang, ID^d Yiyao Chen, ID^e Youwen Pan, ID^a Kangrong Yan, ID^a Chang-Zhi Li, ID^a Minmin Shi, ID^a Lijian Zuo, ID^a Chang-Qi Ma, ID^d Jie Min, ID^c Yujing Liu ID^b * and Hongzheng Chen ID^a*

Intuitive nanoscale visualization of sensitive donor–acceptor (D–A) heterojunction interfaces is still a huge challenge in organic photovoltaics (OPVs) but plays a critical role in carrier management. Herein, nanoscale visualization of the interfaces of newly developed asymmetric non-fullerene acceptors (NFAs) with an ideal absorption edge is realized and some interesting molecular microstructural features, including the alloy-like symbiosis of two NFAs in one domain and curved-crystal behavior in the D:A blend, are uncovered and further correlated with the charge transport and non-radiative loss properties in binary and ternary systems. It is also unveiled that for wide bandgap donor and narrow bandgap acceptor systems, the interfacial bending energy obtained on the ionization potential side is negatively correlated with non-radiative loss in small driving force systems, another factor in manipulating energy loss. Finally, double-channel recombination suppression leads to a record efficiency of 19.3% (certified: 19.3%) for asymmetric acceptor-based quaternary OPVs. This work brings interface research into a new era that enables the discovery of intrinsic interfacial features at under sub-nanometer resolution, thus facilitating intrinsic correlations between molecular microstructure and carrier management.

Received 27th February 2023,
Accepted 4th April 2023

DOI: 10.1039/d3ee00630a

rsc.li/ees

Broader context

Despite the rapid rise in power conversion efficiency (PCE) for organic photovoltaics (OPVs), there is still the main challenge of large non-radiative recombination loss, which hinders the performance of approaching the Shockley–Queisser (SQ) limit. The opportunity to mitigate non-radiative loss may lie in the heterojunction interfaces, a clear picture of which is waiting to be unveiled *via* nanoscale research. Herein, we developed various asymmetric acceptors and performed nanoscale studies on their interfaces, thus uncovering hidden molecular microstructural features, which are further correlated with charge transport and non-radiative loss, and disclosing the critical role of interfacial bending energy in energy loss. With optimized carrier management, a record certified efficiency of 19.3% was achieved for asymmetric acceptor-based OPVs. This work sheds light on solving the energy loss issue and leading OPV research into the nanoscale level.

^a State Key Laboratory of Silicon Materials, International Research Center for X Polymers, Department of Polymer Science and Engineering, Zhejiang University, Hangzhou 310027, P. R. China. E-mail: hzchen@zju.edu.cn

^b College of Materials Science and Engineering, Zhejiang University of Technology, Hangzhou 310014, P. R. China. E-mail: yujingliu@zjut.edu.cn

^c The Institute for Advanced Studies, Wuhan University, Wuhan 430072, P. R. China

^d i-Lab & Printable Electronics Research Centre, Suzhou Institute of Nano-tech and Nano-bionics, Chinese Academy of Sciences, Suzhou 215123, P. R. China

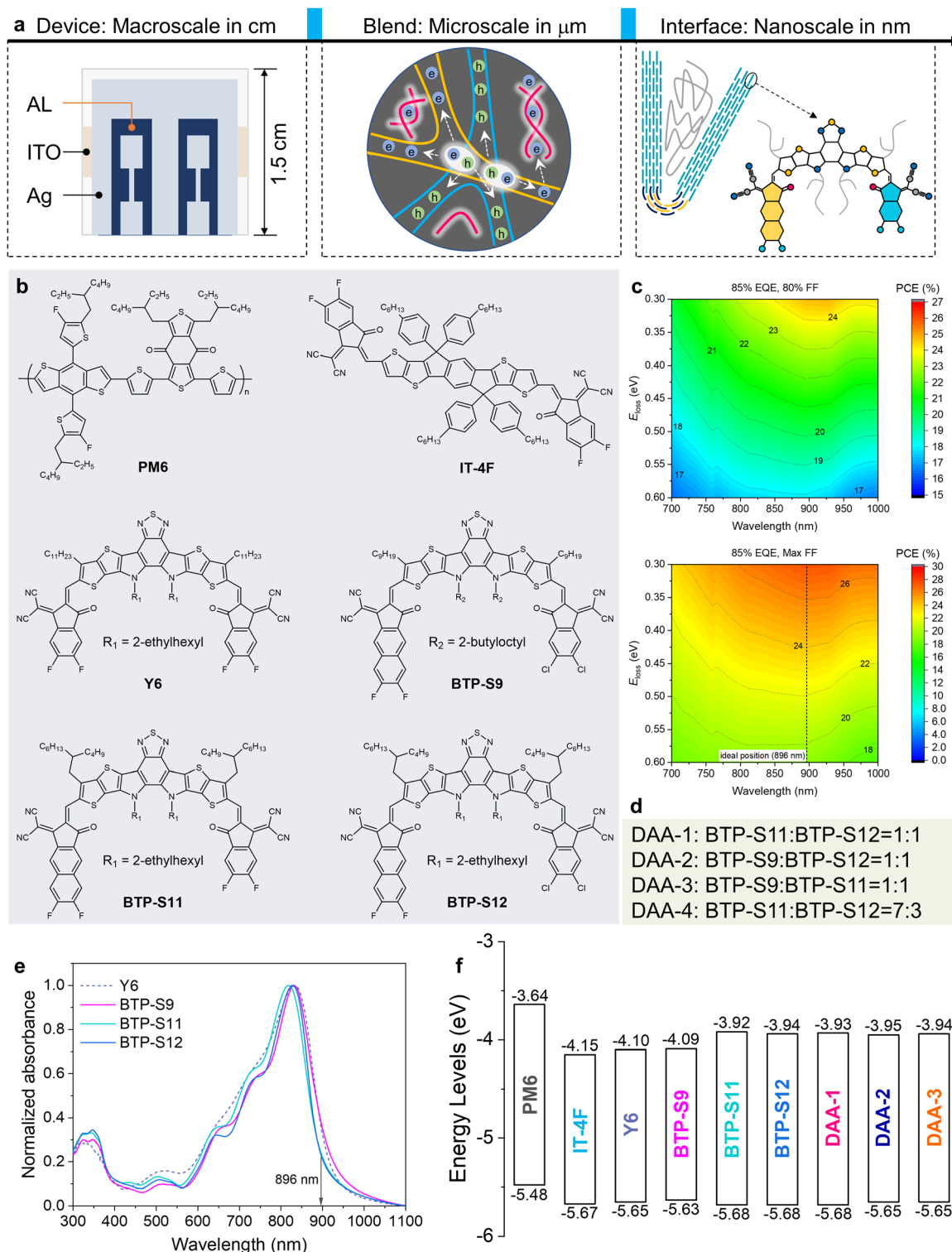
^e Vacuum Interconnected Nanotech Workstation (Nano-X), Suzhou Institute of Nano-Tech and Nano-Bionics, Chinese Academy of Sciences, Suzhou 215123, P. R. China

† Electronic supplementary information (ESI) available: Experimental procedures, NMR spectra, UV-vis, CV, certificate report, mobility, SCLC, contact angle, AFM, DSC, GIWAXS, HR-TEM, FTPS-EQE, UPS, EQE, etc. See DOI: <https://doi.org/10.1039/d3ee00630a>

‡ S. Li, C. He, T. Chen and J. Zheng contributed equally to this work.

Introduction

Single-junction organic photovoltaics (OPVs) based on non-fullerene acceptors (NFAs) have achieved an efficiency of over 19% recently, thanks to the emergence of Y-series molecules with high luminescence and multiple charge transport channels.^{1–13} The continuous increase of efficiency is closely related to the careful management of carrier dynamics, including the processes of charge separation, recombination, transport, and collection.¹⁴ Hence, research at different scales has been performed to disclose and optimize carrier behaviours (Fig. 1(a)). At the macroscopic level, designing suitable buffer layers between the active layer (AL) and electrode and constructing an island-like electrode have been



factor (FF).^{8,19} As a result, both the J_{sc} and FF have progressed significantly toward their Shockley–Queisser (SQ) limits, while open-circuit voltage (V_{oc}) still lags.²⁰ The large V_{oc} loss is mainly caused by the existence of disadvantageous non-radiative recombination loss.^{21–23}

One established rule is the approximately linear relationship between non-radiative recombination loss and the energetic offset (ΔE_{LE-CT}), which is the energetic difference between the local exciton (LE) state and the charge transfer (CT) state, but this no longer holds true if the energetic offset is less than 0.1 eV.²⁴ It is thus desirable to explore the rules for mitigating non-radiative recombination loss in small driving force systems ($\Delta E_{LE-CT} < 0.1$ eV).^{25–28}

In OPVs, the donor–acceptor (D–A) heterojunction interfaces are the main locations for the carrier dynamics of charge transfer, separation and recombination and are also where the CT state occurs.²⁹ As non-radiative recombination loss mainly occurs in the CT state, the D–A heterojunction interfaces play a crucial role in affecting non-radiative recombination loss.³⁰ Despite their importance, the D–A heterojunction interfaces remain a mystery, as unveiling the detailed packing behaviors at nanoscale is quite challenging. In previous research, interface studies were mostly performed in indirect ways or at limited resolutions and are thus unable to reveal intrinsic interfacial features, like structural ordering and defects, under sub-nanometer resolution.^{31–33} In addition, a multicomponent strategy introducing extra donor or acceptor components to binary systems is commonly used to improve the carrier dynamics and device parameters, especially in pursuing a higher V_{oc} .^{34–41} However, how the extra component combines with the host materials at the nanoscale level is not yet well understood, building barriers to acquiring design rules for successful multicomponent blends.⁴² In summary, the field of nanoscale study on interfaces is still blank but is critical to the exploration of successful multicomponent systems with comprehensive carrier management, particularly with non-radiative recombination loss mitigation.

In this work, based on a series of asymmetric Y-series NFAs (Fig. 1(b)), besides a traditional macroscale study on the device and a microscale study on the blend, we performed nanoscale visualization on the interfaces of the binary and multicomponent systems, uncovering some interesting molecular microstructural features, including the alloy-like symbiosis of two NFAs in one domain and curved-crystal behavior in the D:A blend, which are further correlated with carrier management, including non-radiative recombination loss and charge transport. Finally, double channel recombination suppression (DCRS) *via* a triple asymmetric acceptor (TAA) strategy enables a highest power conversion efficiency (PCE) of 19.3% (certified 19.3%) with an improved V_{oc} of 0.89 V and an enhanced FF of 80%. This work achieves a visualization study on D/A interfaces under sub-nanometer resolution, thus bringing interface research into a new era.

Results and discussion

Material systems design

According to the SQ limits, there exists an ideal bandgap where the highest potential efficiency can be reached. Designing NFAs

with an absorption edge close to the ideal bandgap is beneficial for solving the trade-off between photovoltage and photocurrent, thus maximizing the efficiency more easily. For example, by utilizing the quinoid resonance effect, Y6 shows an absorption edge (~ 930 nm) closer to the ideal bandgap relative to IT-4F and is thus a current state-of-the-art NFA. For an accurate value of the ideal bandgap, theoretical efficiency calculations were performed, as illustrated in Fig. S1 and Note S1 (ESI†) and depicted in Fig. 1(c). It was found that the ideal absorption wavelength edge is around 896 nm, corresponding to a bandgap of 1.384 eV, which means further modifications should still be performed on Y6 to get a NFA with the ideal bandgap. This also indicated that, under the reasonable set of 85% external quantum efficiency (EQE) and 80% FF, an E_{loss} of 0.506 eV will be required for 20% efficiency based on photovoltaic materials with the ideal bandgap.

Based on the skeleton of Y6, the molecular design strategies of asymmetric terminals, branched alkyl side chains and halogen atom tuning were used, yielding the NFAs BTP-S9, BTP-S11 and BTP-S12 (Fig. 1(b)), among which BTP-S11 and BTP-S12 possess an absorption edge of ~ 896 nm. The synthetic details of the asymmetric acceptors can be found in ESI† (Fig. S2–S7). Based on the above three asymmetric NFAs, a dual asymmetric acceptor (DAA) strategy is proposed for multicomponent study (Fig. 1(d)). The basic absorption and energy level properties of the various NFAs are displayed in Fig. 1(e)–(f) and Fig. S8, S9 (ESI†).

Device performance study

Binary and ternary OPVs were fabricated with the conventional device structure of indium tin oxide (ITO)/poly(3,4-ethylenedioxythiophene) polystyrene sulfonate (PEDOT:PSS)/active layer/bisfulleropyrrolidinium tris(methoxyethoxy) phenyl iodide (Bis-FIMG)/Ag to check the photovoltaic performance (Fig. S10, ESI†). The fabrication details can be found in ESI†. As shown in Fig. 2 and Table 1, binary OPVs based on a PM6:BTP-S11 blend delivered a maximum PCE of 18.9% with a high V_{oc} of 0.878 V, large J_{sc} of 27.1 mA cm^{-2} and outstanding FF of 79.3%, better than the binary OPVs based on PM6:BTP-S12 (PCE of 17.7%) or PM6:BTP-S9 (PCE of 18.8%). The above three binary systems show similar FFs of $\sim 79\%$, comparing favourably with FF variations in ternary systems. The efficiency variations among these three binary systems originate from the change of voltage and photocurrent. The variation trend of voltage conforms to the relationship presented in the lowest unoccupied molecular (LUMO) levels of the relevant NFAs (Fig. 1(f)). The significantly lower photocurrent (25.6 mA cm^{-2}) for PM6:BTP-S12-based OPVs is partly limited by the formation of large domains caused by the strong aggregation of BTP-S12, as discussed below.

For ternary OPVs, a common rule is that compositional dependent voltage variation normally shows a linear relationship,⁴⁰ as seen in the PM6:DAA-3 system (Fig. S11, ESI†). However, neither the PM6:DAA-1 nor the PM6:DAA-2 system follow a linear relationship and some even show higher voltages than the linear values. Correspondingly, an increase in FF is observed in both the PM6:DAA-1 and PM6:DAA-2 systems, but not in the PM6:DAA-3 system (Fig. S12, ESI†), indicating that

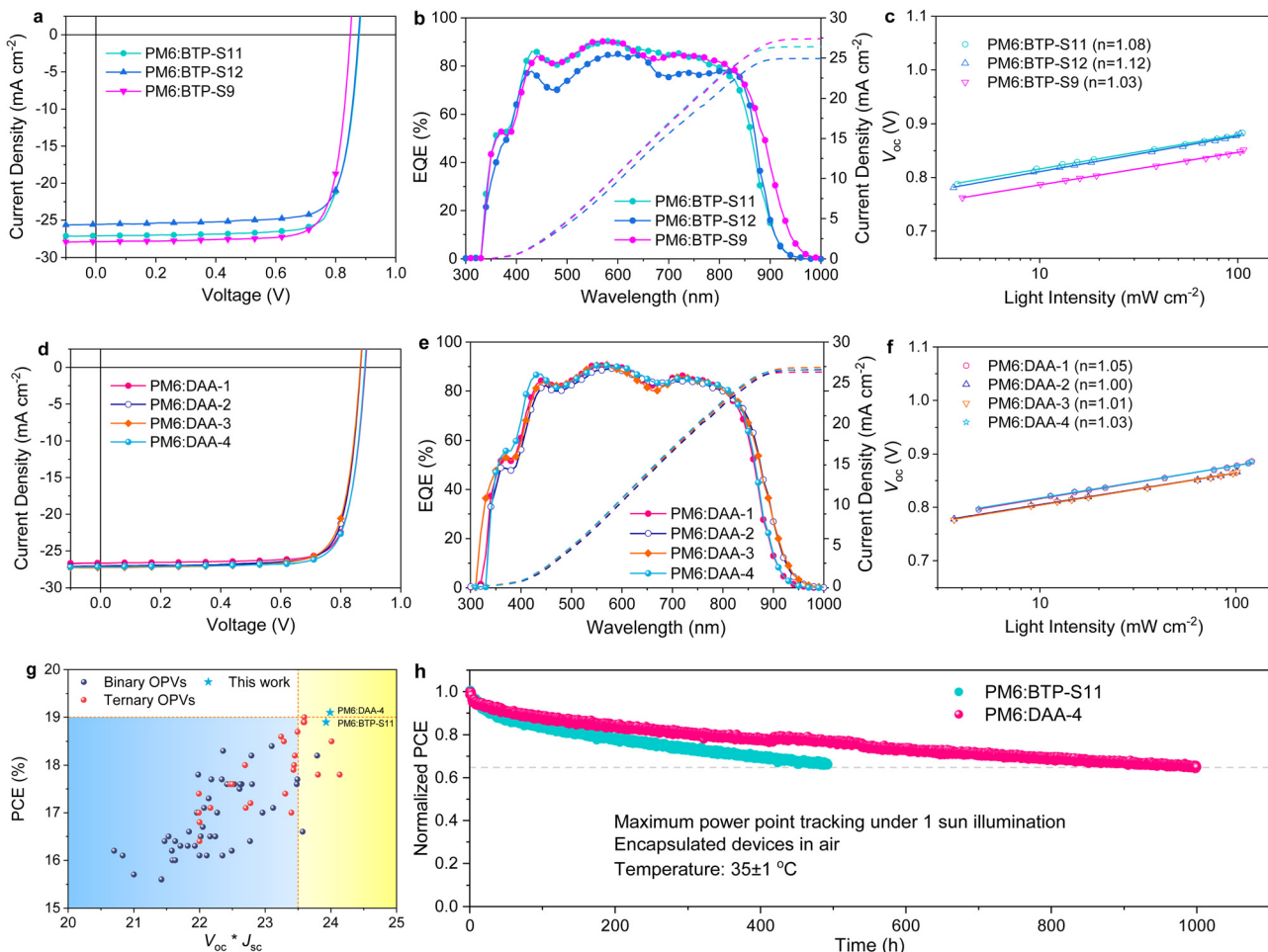


Fig. 2 (a) J – V curves of binary OPVs based on PM6:BTP-S11, PM6:BTP-S12 and PM6:BTP-S9 blends. (b) EQE curves of the relevant binary OPVs. (c) The dependence of V_{oc} on light intensity (P_{light}) for relevant binary OPVs. (d) J – V curves of ternary OPVs based on PM6:DAA-1, PM6:DAA-2, PM6:DAA-3 and PM6:DAA-4 blends (DAA-4 is BTP-S11 : BTP-S12 = 0.7 : 0.3). (e) EQE curves of the relevant ternary OPVs. (f) The dependence of V_{oc} on P_{light} of relevant ternary OPVs. (g) Photovoltaic performance comparison between this work and reported ones. (h) Light stability tests of devices based on PM6:BTP-S11 and PM6:DAA-4 with maximum power point (MPP) tracking under one sun illumination.

Table 1 Summary of photovoltaic parameters for various OPVs

Device type	Active layer ^a	V_{oc} (V)	J_{sc} (mA cm ⁻²)	FF (%)	PCE (%)
Binary	PM6:BTP-S11	0.878 (0.881 ± 0.002)	27.1 (26.8 ± 0.2)	79.3 (79.0 ± 0.4)	18.9 (18.7 ± 0.1)
	PM6:BTP-S12	0.876 (0.877 ± 0.002)	25.6 (25.2 ± 0.3)	78.8 (78.6 ± 0.5)	17.7 (17.3 ± 0.2)
	PM6:BTP-S9	0.849 (0.850 ± 0.001)	27.9 (27.7 ± 0.1)	79.2 (78.7 ± 0.3)	18.8 (18.5 ± 0.1)
Ternary	PM6:DAA-1	0.881 (0.881 ± 0.001)	26.7 (26.6 ± 0.1)	80.0 (79.8 ± 0.2)	18.8 (18.7 ± 0.1)
	PM6:DAA-2	0.866 (0.866 ± 0.001)	27.0 (26.9 ± 0.1)	79.8 (79.8 ± 0.1)	18.7 (18.6 ± 0.1)
	PM6:DAA-3	0.865 (0.866 ± 0.001)	27.3 (27.0 ± 0.1)	78.5 (78.4 ± 0.3)	18.5 (18.3 ± 0.1)
	PM6:DAA-4	0.880 (0.882 ± 0.001)	27.1 (27.0 ± 0.1)	79.9 (79.6 ± 0.2)	19.1 (18.9 ± 0.1)
Quaternary	PM6:TAA-1 ^b	0.890 (0.891 ± 0.002)	27.2 (27.1 ± 0.1)	80.0 (79.6 ± 0.3)	19.3 (19.1 ± 0.1)
	PM6:TAA-1 ^c	0.885	27.5	79.3	19.3

^a The total D:A weight ratio is fixed as 1:1.2. ^b TAA-1 is BTP-S11:BTP-S12:BTP-S2 = 0.7:0.3:0.2. ^c Certified result by National Photovoltaic Industry Metrology and Testing Center, China.

PM6:DAA-1 and PM6:DAA-2 are ternary systems behaving differently from that of PM6:DAA-3.

Subsequently, we optimized the weight ratio of BTP-S11:BTP-S12 composite to 7:3, termed DAA-4, and achieved an

optimized PCE of 19.1% with a V_{oc} of 0.880 V, J_{sc} of 27.1 mA cm⁻² and FF of 79.9%. A full copy of the certification report from the National Photovoltaic Industry Measurement and Testing Center (NPVIM) of China for PM6:DAA-4-based OPVs is provided

as Fig. S13 (ESI[†]). Notably, the $(V_{oc} \times J_{sc})$ values are positively correlated with the PCE values (Fig. 2(g) and Table S1, ESI[†]), as designing photovoltaic materials with an absorption edge close to the ideal bandgap is beneficial for maximizing the $(V_{oc} \times J_{sc})$ values.

EQE tests were synchronously performed to cross-check the photocurrent generation, as shown in Fig. 2(b) and (e). High and broad photoresponses are observed for PM6:BTP-S11 and PM6:BTP-S9-based binary OPVs with the highest EQE values exceeding 90%, with a lower response for the PM6:BTP-S12-based one, which conforms to the J_{sc} values presented in the J - V curves (Fig. 2(a)). The integrated current densities from the EQE curves are found to be 26.39 mA cm^{-2} , 24.93 mA cm^{-2} and 27.40 mA cm^{-2} for the PM6:BTP-S11-based, PM6:BTP-S12-based and PM6:BTP-S9-based OPVs, respectively, with errors of less than 3% of the J_{sc} values (Fig. 2(b)). For the ternary OPVs, the photoresponse intensities are similar and the differences mainly lie in the absorption ranges. The PM6:DAA-4-based OPVs show slightly higher EQE values in the 350–450 nm range than the PM6:DAA-1-based OPVs, enabling the higher current density detected in the J - V curves (Fig. 2(d)). The integrated current densities are calculated to be 26.30 mA cm^{-2} , 26.59 mA cm^{-2} , 26.87 mA cm^{-2} and 26.56 mA cm^{-2} for the PM6:DAA-1-based, PM6:DAA-2-based, PM6:DAA-3-based and PM6:DAA-4-based OPVs with errors within 2% of the J_{sc} values (Fig. 2(e)).

Light intensity variation measurements were conducted to examine the charge recombination situations. The relationship between J_{sc} and light intensity (P_{light}) can be expressed as $J_{sc} \propto P_{light}^{\alpha}$. For both the binary and ternary OPVs, the α values all approach 1, indicating similar situations in bimolecular recombination (Fig. S14, ESI[†]). The relationship between V_{oc} and P_{light} can be expressed as $V_{oc} \propto nkT/q\ln(P_{light})$. Similarly, only minor differences are presented among the ideal factor values of n , which are all close to 1 (Fig. 2(c) and (f)).

Long-term light stability with maximum power point (MPP) tracking under 1 sun illumination was tested for the best binary OPV PM6:BTP-S11 and the best ternary OPV PM6:DAA-4. As shown in Fig. 2(h), the ternary OPV shows a shorter burn-in region and a better long-term linear decay region than the binary OPV, with 65% initial efficiency maintained after 1000 h illumination at MPP condition, implying that the ternary blend effectively improves the device stability.

The charge transport property was examined by the space-charge limited current (SCLC) method. The results are plotted in Fig. S15 (ESI[†]) and summarized in Table S2 (ESI[†]). Among the three binary systems, both the PM6:BTP-S11-based and PM6:BTP-S9-based devices show higher hole (μ_h) and electron (μ_e) mobilities and also more balanced μ_h/μ_e ratios than the PM6:BTP-S12-based one. Among the four ternary systems, the PM6:DAA-1-based device retains a high μ_h comparable to that of the PM6:BTP-S11-based one and acquires a higher μ_e than the binary systems of PM6:BTP-S11 and PM6:BTP-S12. However, both μ_h and μ_e are negatively affected in the PM6:DAA-2-based and PM6:DAA-3-based devices compared with their relevant binary ones. The benefits in mobility for the PM6:DAA-1-based OPV might contribute to the achievement of a higher FF relative

to the PM6:DAA-2- and PM6:DAA-3-based OPVs. For the PM6:DAA-4-based device, both μ_h and μ_e are simultaneously enhanced, thus endowing a higher PCE relative to that of the PM6:DAA-1-based one.

Blend property study

To identify the blend properties, we performed multiple characterizations from the aspects of miscibility, aggregation, thermal property, and crystallinity. For miscibility, through contact angle experiments (Fig. S16 and Table S3, ESI[†]), a higher Flory-Huggins interaction parameter (χ) was found between PM6 and BTP-S9 relative to BTP-S11 and BTP-S12, indicating that alkyl side-chain induced molecular packing evolution is effective for miscibility tuning.⁴ Furthermore, a reduced miscibility was also presented between PM6 and DAA-1 relative to BTP-S11 and BTP-S12, which differs from DAA-2 or DAA-3, implying a ternary blend as another feasible way for miscibility tuning.⁴³ For aggregation, through atomic force microscopy (AFM) images (Fig. S17 and S18, ESI[†]), except for BTP-S12 which shows a strong aggregation tendency, all the other films possess relatively smooth surfaces with a small roughness of 0.5–0.7 nm. For the thermal property, differential scanning calorimetry (DSC) measurements were conducted (Fig. S19, ESI[†]). BTP-S9, BTP-S11 and BTP-S12 have three different melting points (307.1 °C for BTP-S9, 315.1 °C for BTP-S11 and 329.1 °C for BTP-S12). For DAA-2 and DAA-3, two melting points appear and move to a lower temperature range relative to the relevant single acceptors. For DAA-1, only one melting point (312.8 °C), which differs from those of BTP-S11 and BTP-S12, was observed. The above thermal property variations imply that DAA-1 possibly works as an alloy-like model more than DAA-2 and DAA-3. For crystallinity, grazing-incidence wide-angle X-ray scattering (GIWAXS) measurements were performed and the results are displayed in Fig. S20–S24 (ESI[†]). Both BTP-S11 and BTP-S12 show a π - π stacking peak at $q = 1.75 \text{ \AA}^{-1}$ ($d = 3.59 \text{ \AA}$) in the out-of-plane direction and a lamellar peak at $q = 0.43 \text{ \AA}^{-1}$ ($d = 14.60 \text{ \AA}$) in the in-plane direction; for BTP-S9, the π - π stacking peak in the out-of-plane direction moves to $q = 1.76 \text{ \AA}^{-1}$ ($d = 3.57 \text{ \AA}$) and the lamellar peak in the in-plane direction moves to $q = 0.40 \text{ \AA}^{-1}$ ($d = 15.70 \text{ \AA}$). All the NFAs adopt a face-on orientation and possess good crystallinity. For the binary blends, high crystallinity is retained in the PM6:BTP-S9 and PM6:BTP-S11 systems, but not in PM6:BTP-S12, which explains why the PM6:BTP-S12 system shows lower mobilities and worse performance, as shown above. For the ternary blends, PM6:DAA-1 shows higher crystallinity than the PM6:DAA-2 and PM6:DAA-3 systems. In addition, the π - π stacking peak of PM6:DAA-1 film is located at $q = 1.74 \text{ \AA}^{-1}$ ($d = 3.61 \text{ \AA}$), a bit tighter than those of the PM6:DAA-2 and PM6:DAA-3 films ($q = 1.73 \text{ \AA}^{-1}$, $d = 3.63 \text{ \AA}$). The PM6:DAA-4 system is similar to the PM6:DAA-1 system.

Molecular microstructure visualization

To directly observe the molecular interfaces with angstrom-level resolution, high resolution transmission electron microscopy (HR-TEM) technology was applied. As shown in Fig. 3, BTP-S11 shows an interplanar crystal spacing ranging from 0.20 to 0.25 nm, smaller than that of BTP-S12 (0.26–0.29 nm), a

typical feature to distinguish between these two NFAs' crystalline regions. In the DAA-1 film, BTP-S11 and BTP-S12 coexist in one domain of ~ 50 nm instead of forming individual crystalline domains. This phenomenon, where two NFAs co-crystallize edge-to-edge to form one homogenous domain, is termed alloy-like symbiosis. It was also found that such alloy-like symbiosis renders the formation of spherocrystals with exceptionally high crystallinity. As shown in Fig. S25 (ESI[†]), BTP-S9 possesses a larger interplanar crystal spacing of ~ 0.35 nm. When BTP-S9 and BTP-S12 are mixed to form DAA-2, the alloy-like symbiosis phenomenon can still be observed but is not as distinct as in DAA-1. When BTP-S9 and BTP-S11 are mixed to form DAA-3, the alloy-like symbiosis phenomenon disappears, probably due to the large discrepancy (>0.1 nm) in the interplanar crystal spacings of the two molecules. This alloy-like symbiosis may explain why the PM6:DAA-1 and PM6:DAA-2 systems acquire an enhancement in FF, but the PM6:DAA-3 system does not. It seems that lattice matching is one of the prerequisites for forming alloy-like symbiosis and an interplanar crystal spacing difference of no more than 0.1 nm between the two NFAs is preferred. To further confirm our supposition, another asymmetric NFA BTP-15 with four chlorine atoms was synthesized for study (Fig. S26, ESI[†]), as it has a significantly large interplanar crystal spacing of ~ 0.45 nm (Fig. S27, ESI[†]). When BTP-S9 and BTP-S15 are blended to form DAA-5 (BTP-S9 : BTP-S15 = 1 : 1), no alloy-like symbiosis domains are identified, while an individual large domain is formed for BTP-S9/BTP-S15 itself, certifying the importance of lattice matching in the formation of alloy-like symbiosis. As a result, reduced J_{sc}

and FF values were observed in the PM6:DAA-5-based ternary device relative to those of the PM6:BTP-S9-based binary device, similar to that observed in the PM6:DAA-3 system (Fig. S28, ESI[†]).

Then, we studied the molecular microstructure in D:A blends, as shown in Fig. 3 and Fig. S29 (ESI[†]). Relatively, the NFAs show a higher crystallinity than PM6 and their features can thus be observed in the D:A blends more easily. Surprisingly, a new curved-crystal phenomenon from the NFAs was observed, connecting with the straight crystal in a uniform interplanar crystal spacing, especially in the PM6:BTP-S9 and PM6:BTP-S11 systems. Such a curved crystal only appears in the D:A blends and cannot be found in the neat donor or acceptor films, implying its formation may be related to the molecular interaction between D and A. Curved crystal is beneficial for creating sufficient D/A interfaces for charge separation, but also risks forming more CT states, thus providing more opportunities for the formation of non-geminate triplet CT states that normally recombine in a non-radiative way.^{44,45} In the PM6:DAA-1 system, the curved-crystal behavior is relieved to some extent, which further affects the non-radiative recombination loss mitigation, as revealed below. Further, the relief of curved-crystal behavior in the PM6:DAA-1 blend might be from the reduced miscibility and formed spherocrystals demonstrated above.

Energy loss analysis

To explain the different voltage variation trends in the ternary OPVs, we performed detailed energy loss analyses for the binary and ternary OPVs studied in this work. The relevant results are

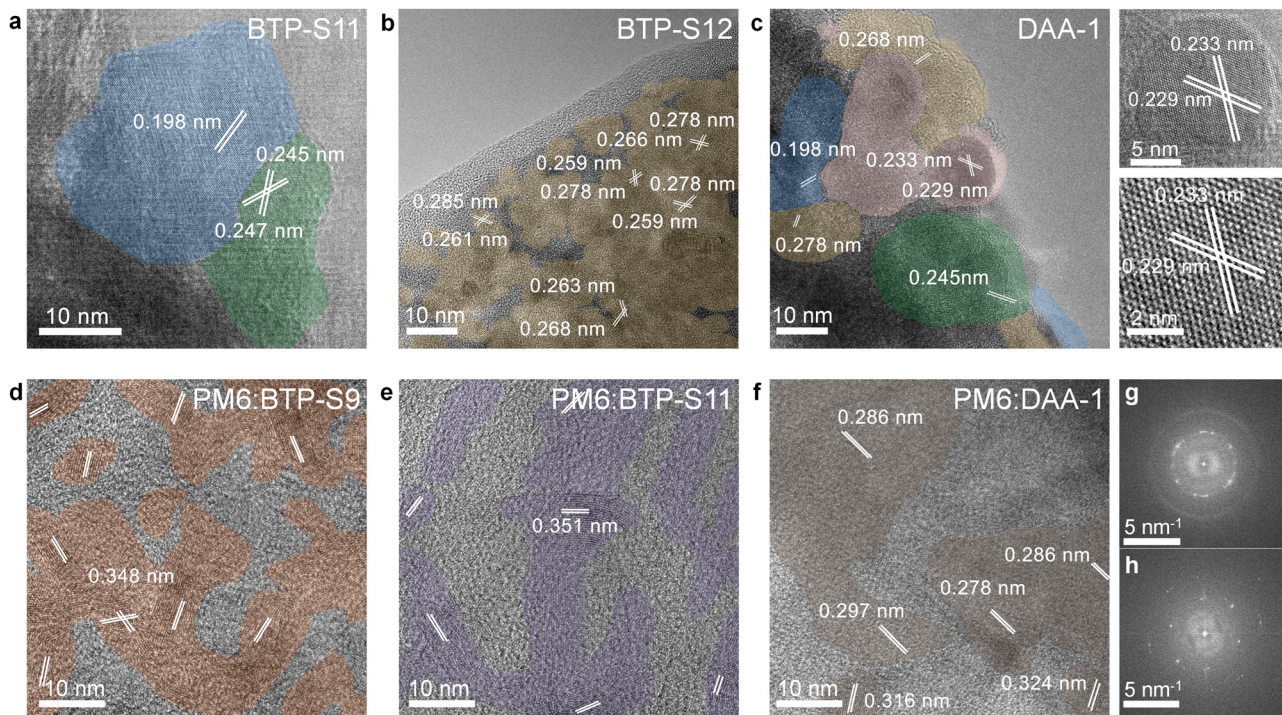


Fig. 3 (a)–(c) High resolution transmission electron microscopy (HR-TEM) images of BTP-S11 (a), BTP-S12 (b), and DAA-1 (c) films. (d)–(f) HR-TEM images of PM6:BTP-S9 (d), PM6:BTP-S11 (e), and PM6:DAA-1 (f) films. (g) Fast Fourier transform (FFT) of the image from (e) for PM6:BTP-S11 film. (h) FFT of the image from (f) for PM6:DAA-1 film. Colors are attached to the crystalline regions with the programmed software and change to distinguish various interplanar crystal spacing and domain edges.

displayed in Fig. 4 and the detailed parameters are summarized in Table 2. We determined the bandgaps *via* the integral method of EQE curves (Fig. S30, ESI[†]), which considers effects from both the absorption of active layer materials and the whole device, by applying eqn (1)⁴⁶

$$E_g = \frac{\int_a^b E_g P(E_g) dE_g}{\int_a^b P(E_g) dE_g} \quad (1)$$

where the integration limits a and b were chosen as $P(a) = P(b) = 0.5\text{Max}[P(E_g)]$. Among the three parts of energy loss, *i.e.*, radiative recombination loss above the bandgap (ΔE_1), radiative recombination loss below the bandgap (ΔE_2) and non-radiative recombination loss (ΔE_3), ΔE_3 is currently the most significant one to conquer to acquire a lower E_{loss} . The factor that determines the value of ΔE_3 is the electroluminescence quantum efficiency (EQE_{EL}) of the device, from which ΔE_3 can be calculated through eqn (2)⁴⁷

$$\Delta E_3 = -kT \ln(\text{EQE}_{\text{EL}}) \quad (2)$$

where k is the Boltzmann constant and T is the temperature in Kelvin.

The three binary OPVs exhibit various EQE_{EL} values of $3\text{--}4 \times 10^{-2}\%$, giving ΔE_3 values of 0.194 eV for the PM6:BTP-S11 device, 0.210 eV for the PM6:BTP-S12 device and 0.201 eV for the PM6:BTP-S9 device (Table 2). However, we observe two different phenomena in the luminescence properties of the three ternary OPVs. For the PM6:DAA-3-based device, the EQE_{EL} value ($3.62 \times 10^{-2}\%$) lies between those of the PM6:BTP-S11-based and PM6:BTP-S9-based ones, which is a normal result. But, exceptional (over two times) enhancements in EQE_{EL} values are found for the PM6:DAA-1-based ($8.67 \times 10^{-2}\%$) and PM6:DAA-2-based ($6.38 \times 10^{-2}\%$) devices relative to the relevant binary ones, thus enabling specifically low ΔE_3 values of 0.179 eV for the PM6:DAA-1-based device and 0.190 eV for the PM6:DAA-2-based device. Such obvious luminescence enhancement in the PM6:DAA-1-based and PM6:DAA-2-based ternary OPVs is likely partly responsible for the non-linear voltage variation (Fig. S11, ESI[†]).

To explain the variations in ΔE_2 , we compare the energetic disorders in these binary and ternary systems by extracting the Urbach energy (E_U) through exponential fitting of the Fourier transform photocurrent spectroscopy (FTPS)-EQE curves. The results can be found in Fig. S31 and S32 (ESI[†]).

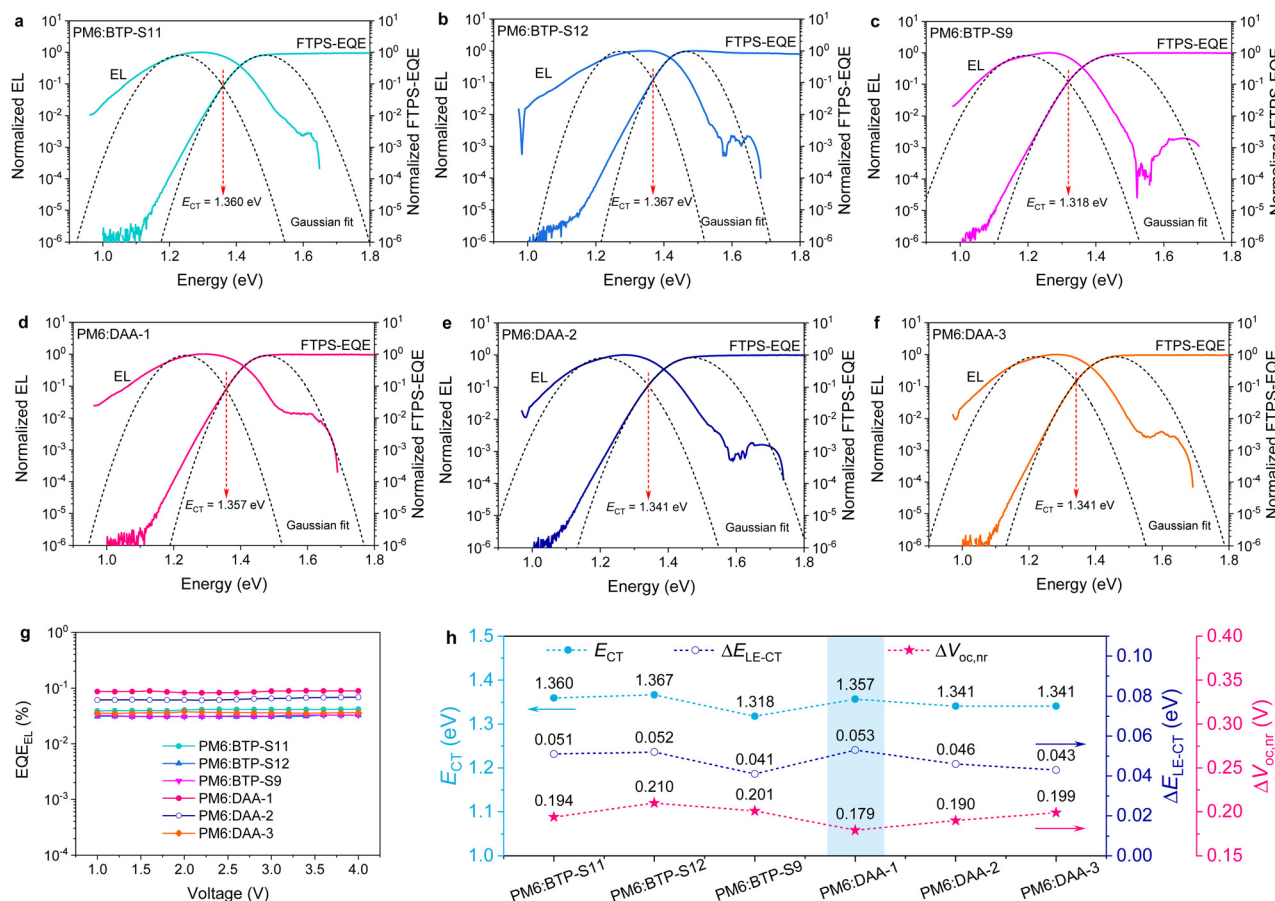


Fig. 4 (a)–(f) Semilogarithmic plots of normalized EL and normalized FTPS-EQE (solid lines) and determination of E_{CT} via Gaussian fits to EL and FTPS-EQE spectra according to the Marcus equation (dashed lines). (g) The EQE_{EL} of devices based on the three binary blends of PM6:BTP-S11, PM6:BTP-S12 and PM6:BTP-S9 and the three ternary blends of PM6:DAA-1, PM6:DAA-2 and PM6:DAA-3. (h) Comparison of E_{CT} , $\Delta E_{\text{LE-CT}}$ and $\Delta V_{\text{oc,nr}}$ for relevant binary and ternary OPVs.

Table 2 Detailed energy losses of the OPVs based on PM6:NFA

Active layer	E_g (eV)	V_{oc}^{SO} (V)	V_{oc}^{rad} (V)	ΔE_1 (eV)	ΔE_2 (eV)	ΔE_3 (eV)	E_{loss} (eV)	EQE _{EL} (%)
PM6:BTP-S11	1.425	1.168	1.075	0.257	0.093	0.194	0.544	4.12×10^{-2}
PM6:BTP-S12	1.409	1.155	1.086	0.254	0.069	0.210	0.533	3.12×10^{-2}
PM6:BTP-S9	1.379	1.128	1.050	0.251	0.078	0.201	0.530	3.17×10^{-2}
PM6:DAA-1	1.425	1.171	1.060	0.254	0.111	0.179	0.544	8.67×10^{-2}
PM6:DAA-2	1.393	1.142	1.056	0.251	0.086	0.190	0.527	6.38×10^{-2}
PM6:DAA-3	1.378	1.122	1.064	0.256	0.058	0.199	0.513	3.62×10^{-2}

Among the three binary systems, the PM6:BTP-S12-based device possesses the lowest E_U of 21.67 meV and also the lowest ΔE_2 of 0.069 eV, implying that the relationship between E_U and ΔE_2 is positively related. Similarly, the PM6:DAA-3-based device has the lowest E_U of 21.84 meV and also the lowest ΔE_2 of 0.058 meV. In addition, the PM6:DAA-1-based device presents a reduced E_U of 22.48 meV relative to the PM6:BTP-S11-based one ($E_U = 23.06$ meV).

The CT state plays an important role during the working of OPVs, affecting charge recombination and charge separation.³⁰ We determine the CT states for these binary and ternary OPVs by performing Gaussian fits to the FTPS-EQE and EL curves *via* the Marcus Equations,⁴⁸

$$EQE_{PV}(E) = \frac{f}{E\sqrt{4\pi\lambda kT}} \exp\left(-\frac{(E_{CT} + \lambda - E)^2}{4\lambda kT}\right) \quad (3)$$

and

$$EQE_{EL}(E) = \frac{Ef}{\sqrt{4\pi\lambda kT}} \exp\left(-\frac{(E_{CT} - \lambda - E)^2}{4\lambda kT}\right) \quad (4)$$

where f is a parameter associated with the electronic coupling matrix element, λ is the reorganization energy related to the CT absorption process and E_{CT} is the free energy difference between the charge transfer complex (CTC) ground state and the CT excited state. Then, the energetic offset (ΔE_{LE-CT}), defined as the difference between the lowest LE state and the lowest CT state, can be calculated for these OPVs. Here, E_{LE} values are obtained *via* the intersection of the EL and FTPS-EQE curves. The comparisons of E_{CT} , ΔE_{LE-CT} and non-radiative voltage loss ($\Delta V_{oc,nr}$) are displayed in Fig. 4(h). First, we can see that all these OPVs are small driving force systems with ΔE_{LE-CT} values varying between 0.04 and 0.05 eV. The relationship between ΔE_{LE-CT} and $\Delta V_{oc,nr}$ no longer follows a simple linear dependence in small driving force systems,²⁴ indicating that some other hidden factors, besides the well-known ΔE_{LE-CT} , may also play an important role in determining non-radiative recombination loss in small driving force systems.

Interfacial bending energy

As shown in Fig. 5(a), for large driving force systems ($\Delta E_{LE-CT} > 0.1$ eV), the large-enough energetic offset drives the Boltzmann equilibrium between the LE and CT states as the dominant way to determine the CT state ratio. Under this precondition, when the stationary state of the reaction between the LE and CT states is reached, the equilibrium constant K can be obtained as

follows.²⁸

$$K = \frac{g_2}{g_1} \exp\left(\frac{\Delta E_{LE-CT}}{kT}\right) \quad (5)$$

Thus, narrowing ΔE_{LE-CT} reduces the K value, giving a lower CT state ratio and lower ΔE_3 . However, for small driving force systems ($\Delta E_{LE-CT} < 0.1$ eV), the above results show that ΔE_3 is not simply decided by the lone factor of ΔE_{LE-CT} . A possible approach for resolving this puzzle is to take an extra process, from the LE state to a charge separation (CS) state, into consideration in the Boltzmann equilibrium (Fig. 5(a)). Such a process directly from the LE to CS states for Y-series NFAs has been confirmed in previous research.⁴⁹⁻⁵¹ If we consider both processes of LE-CT and LE-CS in the Boltzmann equilibrium, when the stationary state of the reaction is reached, the modified equilibrium constant K' will be obtained by

$$K' = \frac{1}{g_{12} \exp\left(-\frac{\Delta E_{LE-CT}}{k_B T}\right) + g_{32} \exp\left(-\frac{\Delta E_{CS-CT}}{k_B T}\right)} \quad (6)$$

where $g_{12} = g_1/g_2$ and $g_{32} = g_3/g_2$. From the above equation, we learn that the reduction of K' is determined by both ΔE_{LE-CT} and ΔE_{CS-CT} (the dissociation energy of the CT state). So, in addition to ΔE_{LE-CT} , ΔE_{CS-CT} also plays an important role in affecting the CT state ratio, thus influencing the non-radiative recombination loss. More detailed analysis for the above conclusion can be found in Note S2 (ESI†). Therefore, factors affecting ΔE_{CS-CT} may be responsible for non-radiative loss mitigation in small driving force systems.

Next, we explore the factors existing at the D/A interfaces that affect ΔE_{CS-CT} . As shown in Fig. 5(b), an energy level bending phenomenon exists at the D/A interfaces, caused by the electrostatic interaction of charges with the quadrupole moments of surrounding molecules.⁵² The energy level bending phenomenon results in an important parameter named interfacial bending energy (B), through which we can identify the following relationship between ΔE_{CS-CT} and B .

$$\Delta E_{CS-CT} = E_{CS} - E_{CT} = E_{Coulomb}^{CT} - B \quad (7)$$

Through the above equation, we learn that ΔE_{CS-CT} and B are negatively related, *i.e.*, enlarging the value of B reduces ΔE_{CS-CT} (see analysis in Note S3, ESI†). The parameter B could be the factor that is responsible for the non-radiative loss mitigation in small driving force systems.

To calculate the value of B , we measured the ionization potential (IP) levels for all donors and acceptors (Fig. S33 and

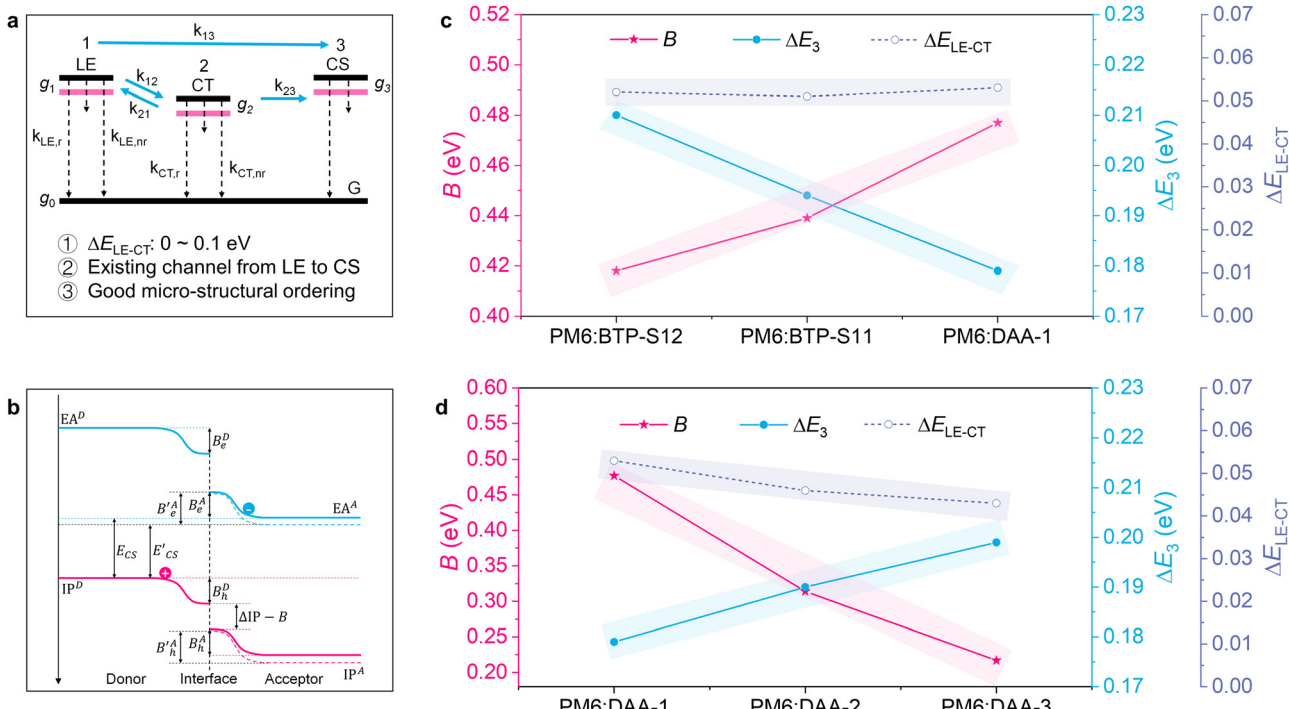


Fig. 5 (a) Diagram of kinetic process involved with LE, CT and CS states. G: ground state, LE: local exciton state, CT: charge transfer state, CS: charge separation state, $g_1/g_2/g_3$: different degeneracies, $k_{LE,r}$: radiative loss rate from LE state, $k_{LE,nr}$: non-radiative loss rate from LE state, $k_{CT,r}$: radiative loss rate from CT state, $k_{CT,nr}$: non-radiative loss rate from CT state, $k_{12}/k_{21}/k_{13}/k_{23}$: conversion rates among different states. (b) Schematic of energy level bending at the donor/acceptor interface. IP: ionization potential, EA: electron affinity, B: energy level bending energy. (c) Relationships among B, ΔE_3 and ΔE_{LE-CT} for PM6:BTP-S12-, PM6:BTP-S11- and PM6:DAA-1-based OPVs. (d) Relationships among B, ΔE_3 and ΔE_{LE-CT} for PM6:DAA-1-, PM6:DAA-2- and PM6:DAA-3-based OPVs.

S34, ESI[†]) with which the value of B can be obtained through the following equation.

$$B = \Delta IP - \Delta E_{LE-CT} \quad (8)$$

The relevant results are analyzed in Note S4 (ESI[†]) and summarized in Table S4 (ESI[†]). We plotted the relationships among ΔE_3 , ΔE_{LE-CT} and B, shown in Fig. 5(c) and (d), for various systems. As shown in Fig. 5(c), the PM6:BTP-S12, PM6:BTP-S11 and PM6:DAA-1 systems possess nearly the same ΔE_{LE-CT} values and, with an increase in B, ΔE_3 is gradually reduced. As displayed in Fig. 5(d), for the three ternary systems, a gradually reduced ΔE_{LE-CT} value does not result in the reduction of ΔE_3 ; correspondingly, a gradually increased B value will lead to a reduced ΔE_3 . The above results uncover the correlation that the interfacial bending energy of B is negatively correlated with the non-radiative recombination loss of ΔE_3 for small driving force systems. Thus, besides reducing energetic offset, enlarging the interfacial bending energy is another feasible approach for mitigating non-radiative recombination loss in small driving force systems.

Correlation analysis

During the process of exciton changing to free charge, one possible channel is LE-CT-CS, in which non-radiative recombination loss can be mitigated *via* tuning the CT state for a

reduced ΔE_{LE-CT} . For classification, this recombination suppression is named “channel I recombination suppression” here. Another possible channel is LE-CS, in which non-radiative recombination loss can be mitigated *via* tuning the interfacial bending energy for a reduced ΔE_{CS-CT} , as revealed in this work. This recombination suppression is named “channel II recombination suppression” here. To check whether double-channel recombination suppression (DCRS) is possible, another asymmetric NFA of BTP-S2 (Fig. S35, ESI[†]), which allows a higher CT state energy ($E_{CT} = 1.444$ eV) and a narrower energetic offset ($\Delta E_{LE-CT} = 0.039$ eV) in the PM6:BTP-S2-based device (Fig. S36, ESI[†]), was introduced to DAA-4, yielding TAA-1 (BTP-S11 : BTP-S12 : BTP-S2 = 0.7 : 0.3 : 0.2).³ Fig. 6(a) shows the J-V curves of the three types of OPVs (binary, ternary and quaternary) and Fig. 6(b) compares the photovoltaic parameters among the three types of OPVs. The photovoltaic parameters of quaternary OPVs are also summarized in Table 1.

It was found that V_{oc} further increased to 0.89 V in the quaternary OPVs while J_{sc} and FF were maintained as high as those of the PM6:DAA-4-based ternary OPVs, leading to an improved PCE of 19.3%, which is the highest efficiency reported to date for asymmetric acceptor-based OPVs. The PM6:TAA-1-based device was sent to NPIVIM for certification and a certified PCE of 19.3% was obtained (Fig. S37, ESI[†]). The EQE spectrum of the relevant quaternary device is provided as Fig. S38 (ESI[†]). The above result proves DCRS is feasible for improved device

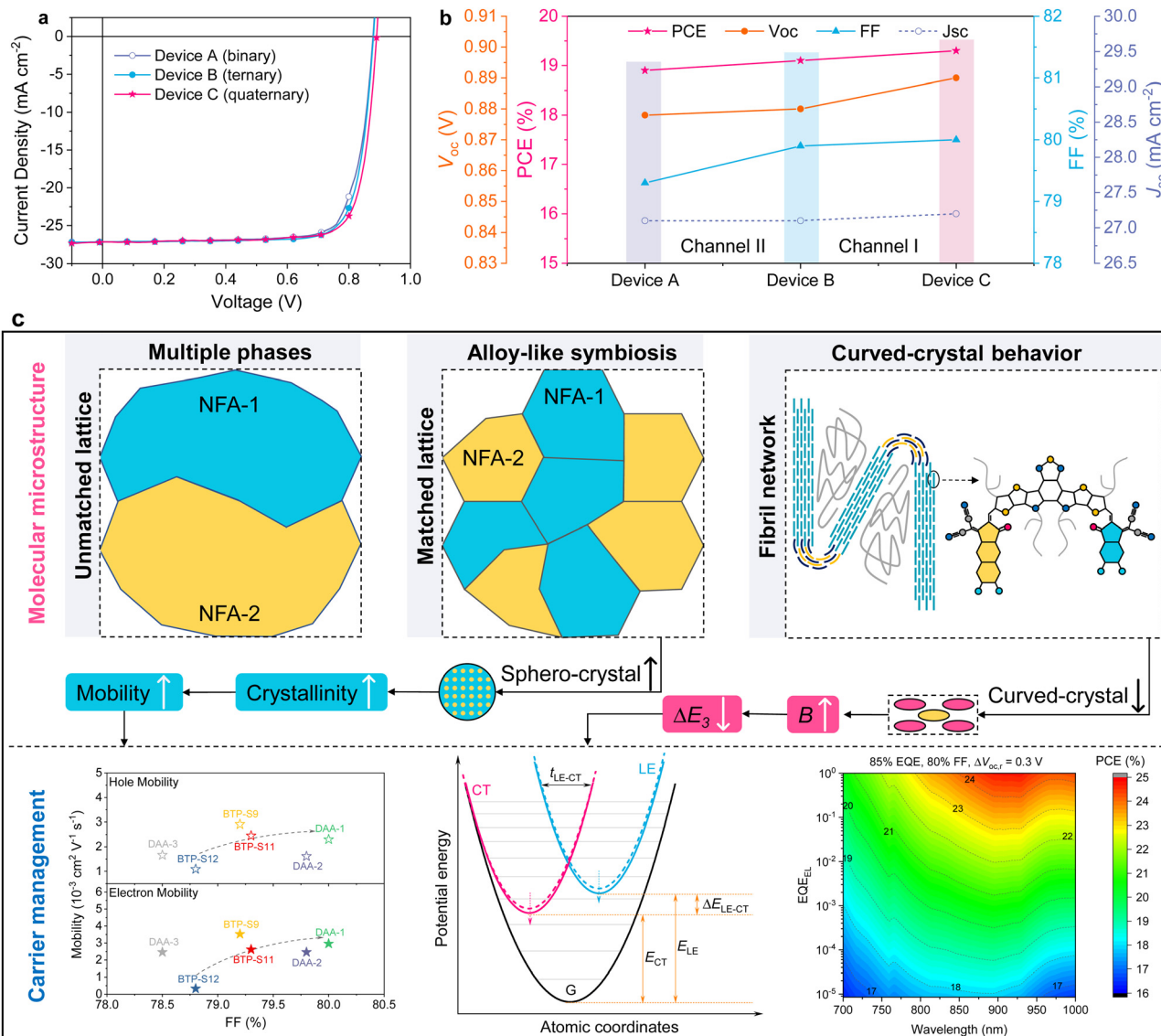


Fig. 6 (a) J – V curves of three types of OPVs (binary, ternary and quaternary). Device A: PM6:BTP-S11, Device B: PM6:DAA-4, Device C: PM6:TAA-1. (b) Comparison of photovoltaic parameters among three types of OPVs. (c) Correlation between molecular microstructure and carrier management.

performance. As to the photovoltaic parameter variation, although channel I and channel II affect both V_{oc} and FF, “channel I recombination suppression” benefits the V_{oc} more, while “channel II recombination suppression” benefits the FF more (Fig. 6(b)).

Finally, we perform correlation analysis between the molecular microstructure and carrier management. As shown in Fig. 6(c), in multicomponent systems, when two NFAs are blended together, if they have unmatched lattices (average interplanar crystal spacing difference >0.1 nm, as measured with HR-TEM), it will be difficult for the two different types of NFA crystals to integrate into the same domain during the course of crystallization; thus, the formation of multiple phases will be preferred. If they have matched lattice spacings (average interplanar crystal spacing difference <0.05 nm), two different NFAs will first crystallize individually to form small-sized

crystals (~ 10 nm), then fuse edge-to-edge when these two types of small-sized crystals meet to form a homogeneous large domain, thus forming alloy-like symbiosis. Alloy-like symbiosis is beneficial for the formation of spherocrystals which help reduce the miscibility with the donor (Fig. S16, ESI[†]) and enhance crystallinity (Fig. S20–S24, ESI[†]). As a result, the charge transport property is promoted, leading to an improved FF.

When a polymer donor is blended with the NFAs, curved-crystal behavior from the NFAs appears at the D:A heterojunction interfaces, which act as bridges for constructing a fibril network. The existence of curved-crystal behavior creates more interfaces for charge separation, but also risks forming more CT states. Alloy-like symbiosis reduces the curved-crystal behavior to some extent, leads to enhanced crystallinity, and promotes intermolecular interaction and better mesoscale structural ordering, thus positively affecting the electrostatic interaction of charges with

the enhanced quadrupole moment (Fig. S39, ESI[†]) and thereby enlarging the interfacial bending energy. An enlarged interfacial bending energy reduces $\Delta E_{\text{CS-CT}}$, resulting in non-radiative loss mitigation. The above analysis reveals how molecular microstructural features, like alloy-like symbiosis and curved-crystal behavior, correlate with carrier management, including charge transport property and non-radiative loss mitigation. Furthermore, when the triple asymmetric acceptor strategy is applied, DCRS is achieved, leading to enhancements in both V_{oc} and FF for a higher PCE. In the future, relative to FF, more efforts should be devoted to reducing non-radiative loss and DCRS could be a feasible approach (Fig. S40, ESI[†]).

Conclusions

In this work, we first performed theoretical efficiency calculations and developed asymmetric NFAs with an ideal absorption edge of ~ 896 nm. Then, based on various asymmetric NFAs, besides a traditional macroscale study on the device and a microscale study on the blend, we initiated nanoscale study of the interfaces for binary and multicomponent OPV systems, through which some interesting molecular microstructural features were uncovered, including the alloy-like symbiosis of two NFAs in one domain and curved-crystal behavior in the D:A blend. Next, carrier management, including non-radiative loss and charge transport, was well studied, through which double-channel recombination suppression and the critical role of the interfacial bending energy on non-radiative loss mitigation were unveiled. Finally, the correlation between molecular microstructure and carrier management was made and a record certified efficiency of 19.3% was achieved in asymmetric acceptor-based OPVs with a high V_{oc} of 0.89 V and a high FF of 80%. This work brings interface studies into a new era that opens the door for unveiling intrinsic interfacial features at the sub-nanometer resolution and provides a new strategy of DCRS for carrier management.

Author contributions

S. L. and H. C. conceived the idea and designed the experiments. S. L. synthesized the asymmetric acceptors and performed the theoretical efficiency calculation. C. H. fabricated the binary and ternary devices and performed the related measurements. T. C. fabricated the quaternary devices and performed AFM measurement. J. Z. and Y. L. did the HR-TEM measurement. R. S. and J. M. carried out the energy loss test. J. F., Y. C. and C.-Q. M. did the GIWAXS measurement. C. H., T. C. and Y. P. conducted device fabrication for efficiency certification. K. Y. and C.-Z. L. provided Bis-FIMG. M. S. and L. Z. commented on this work. H. C. supervised the project. The manuscript was mainly written by S. L. and H. C., and all authors commented on the manuscript.

Conflicts of interest

There are no conflicts to declare.

Acknowledgements

This work is supported by the National Natural Science Foundation of China (no. 52127806, 21734008, 52273199, 61721005, 52173185, 52171225, 52102314), National Key Research and Development Program of China (no. 2019YFA0705902), the China Postdoctoral Science Foundation funded project (no. 2022M712737), the Fundamental Research Funds for the Central Universities (no. 226-2022-00133), and Shanxi-Zheda Institute of Advanced Materials and Chemical Engineering (2021SZ-FR001).

Notes and references

- 1 J. Yuan, Y. Zhang, L. Zhou, G. Zhang, H.-L. Yip, T.-K. Lau, X. Lu, C. Zhu, H. Peng, P. A. Johnson, M. Leclerc, Y. Cao, J. Ulanski, Y. Li and Y. Zou, *Joule*, 2019, **3**, 1140–1151.
- 2 Y. Cui, H. Yao, J. Zhang, K. Xian, T. Zhang, L. Hong, Y. Wang, Y. Xu, K. Ma, C. An, C. He, Z. Wei, F. Gao and J. Hou, *Adv. Mater.*, 2020, **32**, 1908205.
- 3 S. Li, L. Zhan, Y. Jin, G. Zhou, T.-K. Lau, R. Qin, M. Shi, C.-Z. Li, H. Zhu, X. Lu, F. Zhang and H. Chen, *Adv. Mater.*, 2020, **32**, 2001160.
- 4 C. Li, J. Zhou, J. Song, J. Xu, H. Zhang, X. Zhang, J. Guo, L. Zhu, D. Wei, G. Han, J. Min, Y. Zhang, Z. Xie, Y. Yi, H. Yan, F. Gao, F. Liu and Y. Sun, *Nat. Energy*, 2021, **6**, 605–613.
- 5 Y. Cui, Y. Xu, H. Yao, P. Bi, L. Hong, J. Zhang, Y. Zu, T. Zhang, J. Qin, J. Ren, Z. Chen, C. He, X. Hao, Z. Wei and J. Hou, *Adv. Mater.*, 2021, **33**, 2102420.
- 6 S. Li, L. Zhan, N. Yao, X. Xia, Z. Chen, W. Yang, C. He, L. Zuo, M. Shi, H. Zhu, X. Lu, F. Zhang and H. Chen, *Nat. Commun.*, 2021, **12**, 4627.
- 7 L. Zhan, S. Li, Y. Li, R. Sun, J. Min, Z. Bi, W. Ma, Z. Chen, G. Zhou, H. Zhu, M. Shi, L. Zuo and H. Chen, *Joule*, 2022, **6**, 662–675.
- 8 L. Zhu, M. Zhang, J. Xu, C. Li, J. Yan, G. Zhou, W. Zhong, T. Hao, J. Song, X. Xue, Z. Zhou, R. Zeng, H. Zhu, C.-C. Chen, R. C. I. MacKenzie, Y. Zou, J. Nelson, Y. Zhang, Y. Sun and F. Liu, *Nat. Mater.*, 2022, **21**, 656–663.
- 9 C. He, Y. Pan, Y. Ouyang, Q. Shen, Y. Gao, K. Yan, J. Fang, Y. Chen, C.-Q. Ma, J. Min, C. Zhang, L. Zuo and H. Chen, *Energy Environ. Sci.*, 2022, **15**, 2537–2544.
- 10 K. Chong, X. Xu, H. Meng, J. Xue, L. Yu, W. Ma and Q. Peng, *Adv. Mater.*, 2022, **34**, 2109516.
- 11 C. He, Z. Chen, T. Wang, Z. Shen, Y. Li, J. Zhou, J. Yu, H. Fang, Y. Li, S. Li, X. Lu, W. Ma, F. Gao, Z. Xie, V. Coropceanu, H. Zhu, J.-L. Bredas, L. Zuo and H. Chen, *Nat. Commun.*, 2022, **13**, 2598.
- 12 J. Wang, P. Xue, Y. Jiang, Y. Huo and X. Zhan, *Nat. Rev. Chem.*, 2022, **6**, 614–634.
- 13 G. Zhang, F. R. Lin, F. Qi, T. Heumüller, A. Distler, H.-J. Egelhaaf, N. Li, P. C. Y. Chow, C. J. Brabec, A. K. Y. Jen and H.-L. Yip, *Chem. Rev.*, 2022, **122**, 14180–14274.
- 14 M. Zhang, L. Zhu, G. Zhou, T. Hao, C. Qiu, Z. Zhao, Q. Hu, B. W. Larson, H. Zhu, Z. Ma, Z. Tang, W. Feng, Y. Zhang, T. P. Russell and F. Liu, *Nat. Commun.*, 2021, **12**, 309.

15 Y. Lin, B. Adilbekova, Y. Firdaus, E. Yengel, H. Faber, M. Sajjad, X. Zheng, E. Yarali, A. Seitkhan, O. M. Bakr, A. El-Labban, U. Schwingenschlögl, V. Tung, I. McCulloch, F. Laquai and T. D. Anthopoulos, *Adv. Mater.*, 2019, **31**, 1902965.

16 J. Yao, B. Qiu, Z.-G. Zhang, L. Xue, R. Wang, C. Zhang, S. Chen, Q. Zhou, C. Sun, C. Yang, M. Xiao, L. Meng and Y. Li, *Nat. Commun.*, 2020, **11**, 2726.

17 C. Cai, J. Yao, L. Chen, Z. Yuan, Z.-G. Zhang, Y. Hu, X. Zhao, Y. Zhang, Y. Chen and Y. Li, *Angew. Chem., Int. Ed.*, 2021, **60**, 19053–19057.

18 Y. Lin, Y. Firdaus, F. H. Isikgor, M. I. Nugraha, E. Yengel, G. T. Harrison, R. Hallani, A. El-Labban, H. Faber, C. Ma, X. Zheng, A. Subbiah, C. T. Howells, O. M. Bakr, I. McCulloch, S. D. Wolf, L. Tsetseris and T. D. Anthopoulos, *ACS Energy Lett.*, 2020, **5**, 2935–2944.

19 M. Zhang, L. Zhu, T. Hao, G. Zhou, C. Qiu, Z. Zhao, N. Hartmann, B. Xiao, Y. Zou, W. Feng, H. Zhu, M. Zhang, Y. Zhang, Y. Li, T. P. Russell and F. Liu, *Adv. Mater.*, 2021, **33**, 2007177.

20 P. K. Nayak, S. Mahesh, H. J. Snaith and D. Cahen, *Nat. Rev. Mater.*, 2019, **4**, 269–285.

21 S. Liu, J. Yuan, W. Deng, M. Luo, Y. Xie, Q. Liang, Y. Zou, Z. He, H. Wu and Y. Cao, *Nat. Photonics*, 2020, **14**, 300–305.

22 J. Yuan, H. Zhang, R. Zhang, Y. Wang, J. Hou, M. Leclerc, X. Zhan, F. Huang, F. Gao, Y. Zou and Y. Li, *Chem.*, 2020, **6**, 2147–2161.

23 S. Li, C.-Z. Li, M. Shi and H. Chen, *ACS Energy Lett.*, 2020, **5**, 1554–1567.

24 X.-K. Chen, D. Qian, Y. Wang, T. Kirchartz, W. Tress, H. Yao, J. Yuan, M. Hülsbeck, M. Zhang, Y. Zou, Y. Sun, Y. Li, J. Hou, O. Inganäs, V. Coropceanu, J.-L. Bredas and F. Gao, *Nat. Energy*, 2021, **6**, 799–806.

25 J. Liu, S. Chen, D. Qian, B. Gautam, G. Yang, J. Zhao, J. Bergqvist, F. Zhang, W. Ma, H. Ade, O. Inganäs, K. Gundogdu, F. Gao and H. Yan, *Nat. Energy*, 2016, **1**, 16089.

26 D. Qian, Z. Zheng, H. Yao, W. Tress, T. R. Hopper, S. Chen, S. Li, J. Liu, S. Chen, J. Zhang, X.-K. Liu, B. Gao, L. Ouyang, Y. Jin, G. Pozina, I. A. Buyanova, W. M. Chen, O. Inganäs, V. Coropceanu, J.-L. Bredas, H. Yan, J. Hou, F. Zhang, A. A. Bakulin and F. Gao, *Nat. Mater.*, 2018, **17**, 703–709.

27 S. Li, L. Zhan, C. Sun, H. Zhu, G. Zhou, W. Yang, M. Shi, C.-Z. Li, J. Hou, Y. Li and H. Chen, *J. Am. Chem. Soc.*, 2019, **141**, 3073–3082.

28 A. Classen, C. L. Chochos, L. Lüer, V. G. Gregoriou, J. Wortmann, A. Osvet, K. Forberich, I. McCulloch, T. Heumüller and C. J. Brabec, *Nat. Energy*, 2020, **5**, 711–719.

29 L. Zhan, S. Li, Y. Li, R. Sun, J. Min, Y. Chen, J. Fang, C.-Q. Ma, G. Zhou, H. Zhu, L. Zuo, H. Qiu, S. Yin and H. Chen, *Adv. Energy Mater.*, 2022, **12**, 2201076.

30 V. Coropceanu, X.-K. Chen, T. Wang, Z. Zheng and J.-L. Brédas, *Nat. Rev. Mater.*, 2019, **4**, 689–707.

31 C. He, Y. Pan, G. Lu, B. Wu, X. Xia, C.-Q. Ma, Z. Chen, H. Zhu, X. Lu, W. Ma, L. Zuo and H. Chen, *Adv. Mater.*, 2022, **34**, 2203379.

32 Y. Cai, Q. Li, G. Lu, H. S. Ryu, Y. Li, H. Jin, Z. Chen, Z. Tang, G. Lu, X. Hao, H. Y. Woo, C. Zhang and Y. Sun, *Nat. Commun.*, 2022, **13**, 2369.

33 Z. Zhou, S. Xu, J. Song, Y. Jin, Q. Yue, Y. Qian, F. Liu, F. Zhang and X. Zhu, *Nat. Energy*, 2018, **3**, 952–959.

34 S. Li, L. Zhan, Y. Li, C. He, L. Zuo, M. Shi and H. Chen, *Small Methods*, 2022, **6**, 2200828.

35 L. Zhan, S. Li, T.-K. Lau, Y. Cui, X. Lu, M. Shi, C.-Z. Li, H. Li, J. Hou and H. Chen, *Energy Environ. Sci.*, 2020, **13**, 635–645.

36 L. Zhan, S. Li, X. Xia, Y. Li, X. Lu, L. Zuo, M. Shi and H. Chen, *Adv. Mater.*, 2021, **33**, 2007231.

37 Y. Cai, Y. Li, R. Wang, H. Wu, Z. Chen, J. Zhang, Z. Ma, X. Hao, Y. Zhao, C. Zhang, F. Huang and Y. Sun, *Adv. Mater.*, 2021, **33**, 2101733.

38 Y. Pan, X. Zheng, J. Guo, Z. Chen, S. Li, C. He, S. Ye, X. Xia, S. Wang, X. Lu, H. Zhu, J. Min, L. Zuo, M. Shi and H. Chen, *Adv. Funct. Mater.*, 2022, **32**, 2108614.

39 P. Bi, S. Zhang, Z. Chen, Y. Xu, Y. Cui, T. Zhang, J. Ren, J. Qin, L. Hong, X. Hao and J. Hou, *Joule*, 2021, **5**, 2408–2419.

40 L. Zuo, S. B. Jo, Y. Li, Y. Meng, R. J. Stoddard, Y. Liu, F. Lin, X. Shi, F. Liu, H. W. Hillhouse, D. S. Ginger, H. Chen and A. K. Y. Jen, *Nat. Nanotechnol.*, 2022, **17**, 53–60.

41 Y. Li, Y. Guo, Z. Chen, L. Zhan, C. He, Z. Bi, N. Yao, S. Li, G. Zhou, Y. Yi, Y. Yang, H. Zhu, W. Ma, F. Gao, F. Zhang, L. Zuo and H. Chen, *Energy Environ. Sci.*, 2022, **15**, 855–865.

42 N. Gasparini, A. Salleo, I. McCulloch and D. Baran, *Nat. Rev. Mater.*, 2019, **4**, 229–242.

43 L. Ye, H. Hu, M. Ghasemi, T. Wang, B. A. Collins, J.-H. Kim, K. Jiang, J. H. Carpenter, H. Li, Z. Li, T. McAfee, J. Zhao, X. Chen, J. L. Y. Lai, T. Ma, J.-L. Bredas, H. Yan and H. Ade, *Nat. Mater.*, 2018, **17**, 253–260.

44 A. J. Gillett, A. Privitera, R. Dilmurat, A. Karki, D. Qian, A. Pershin, G. Lundi, W. K. Myers, J. Lee, J. Yuan, S.-J. Ko, M. K. Riede, F. Gao, G. C. Bazan, A. Rao, T.-Q. Nguyen, D. Beljonne and R. H. Friend, *Nature*, 2021, **597**, 666–671.

45 Z. Chen, X. Chen, Z. Jia, G. Zhou, J. Xu, Y. Wu, X. Xia, X. Li, X. Zhang, C. Deng, Y. Zhang, X. Lu, W. Liu, C. Zhang, Y. Yang and H. Zhu, *Joule*, 2021, **5**, 1832–1844.

46 Y. Wang, D. Qian, Y. Cui, H. Zhang, J. Hou, K. Vandewal, T. Kirchartz and F. Gao, *Adv. Energy Mater.*, 2018, **8**, 1801352.

47 J. Yao, T. Kirchartz, M. S. Vezie, M. A. Faist, W. Gong, Z. He, H. Wu, J. Troughton, T. Watson, D. Bryant and J. Nelson, *Phys. Rev. Appl.*, 2015, **4**, 014020.

48 K. Vandewal, K. Tvingstedt, A. Gadisa, O. Inganäs and J. V. Manca, *Phys. Rev. B: Condens. Matter Mater. Phys.*, 2010, **81**, 125204.

49 L. Zhu, J. Zhang, Y. Guo, C. Yang, Y. Yi and Z. Wei, *Angew. Chem., Int. Ed.*, 2021, **60**, 15348–15353.

50 X. Zhu, G. Zhang, J. Zhang, H.-L. Yip and B. Hu, *Joule*, 2020, **4**, 2443–2457.

51 J. Xu, S. B. Jo, X. Chen, G. Zhou, M. Zhang, X. Shi, F. Lin, L. Zhu, T. Hao, K. Gao, Y. Zou, X. Su, W. Feng, A. K.-Y. Jen, Y. Zhang and F. Liu, *Adv. Mater.*, 2022, **34**, 2108317.

52 S. Karuthedath, J. Gorenflo, Y. Firdaus, N. Chaturvedi, C. S. P. De Castro, G. T. Harrison, J. I. Khan, A. Markina, A. H. Balawi, T. A. D. Peña, W. Liu, R.-Z. Liang, A. Sharma, S. H. K. Paleti, W. Zhang, Y. Lin, E. Alarousu, D. H. Anjum, P. M. Beaujuge, S. De Wolf, I. McCulloch, T. D. Anthopoulos, D. Baran, D. Andrienko and F. Laquai, *Nat. Mater.*, 2021, **20**, 378–384.